


Atomization of misaligned impinging liquid jets


Cite as: Phys. Fluids **33**, 093311 (2021); <https://doi.org/10.1063/5.0061981>

Submitted: 01 July 2021 • Accepted: 18 August 2021 • Published Online: 16 September 2021

Chenwei Zhang (张宸玮),  Zhenyu Zhang (章振宇),  Kun Wu (吴坤), et al.

COLLECTIONS

 This paper was selected as Featured

 This paper was selected as Scilight



View Online



Export Citation



CrossMark

ARTICLES YOU MAY BE INTERESTED IN

[Simulating the effects of misalignment on impinging jet behavior](#)

Scilight **2021**, 381108 (2021); <https://doi.org/10.1063/10.0006302>

[Droplet breakup and coalescence of an internal-mixing twin-fluid spray](#)

Physics of Fluids **33**, 013317 (2021); <https://doi.org/10.1063/5.0030777>

[Numerical simulation of the atomization of liquid transverse jet in supersonic airflow](#)

Physics of Fluids **33**, 052114 (2021); <https://doi.org/10.1063/5.0050520>

Physics of Plasmas Physics of Fluids
Special Topic: Turbulence in Plasmas and Fluids
Submit Today!

Atomization of misaligned impinging liquid jets

Cite as: Phys. Fluids **33**, 093311 (2021); doi: 10.1063/5.0061981

Submitted: 1 July 2021 · Accepted: 18 August 2021 ·

Published Online: 16 September 2021



View Online



Export Citation



CrossMark

Chenwei Zhang (张宸玮),¹ Zhenyu Zhang (章振宇),²  Kun Wu (吴坤),^{2,a)}  Xi Xia (夏溪),³  and Xuejun Fan (范学军)^{2,4}

AFFILIATIONS

¹School of Mechanical Engineering, Beijing Institute of Technology, Beijing 100081, China

²State Key Laboratory of High Temperature Gas Dynamics, Institute of Mechanics, Chinese Academy of Sciences, Beijing 100190, China

³School of Mechanical Engineering, Shanghai Jiao Tong University, Minhang, Shanghai 200240, China

⁴School of Engineering Science, University of Chinese Academy of Sciences, Beijing 100049, China

^{a)} Author to whom correspondence should be addressed: wukun@imech.ac.cn

ABSTRACT

This study numerically investigated the atomization characteristics of misaligned impinging jets, with the misalignment ratio \hat{e} ranging between 0 and 0.2, by employing the volume of fluid method with an adaptive mesh refinement algorithm. The results show that the droplet Sauter mean diameter varies non-monotonically with \hat{e} and reaches the minimum value, which implies the best atomization performance, at $\hat{e} = 0.1$ under operating conditions concerned in the present work. Meanwhile, the moderately misaligned impingement also leads to a more uniform spatial dispersion of the atomized fragments and droplets. These unique spray behaviors can be attributed to the instability and disintegration of the liquid sheet formed upon jet impingement, as evident from the non-monotonic dependence of the breakup length of the liquid sheet on the misalignment ratio \hat{e} . Analyses on the velocity fluctuation and vorticity distribution further suggest that the misalignment alters the intrinsic instability mode of the liquid sheet by introducing a lateral stretch effect, which diverts the peak streamwise momentum away from the centerline. The current finding indicates that misalignment tuning could be a promising optimization and control technique in propellant mixing and atomization.

Published under an exclusive license by AIP Publishing. <https://doi.org/10.1063/5.0061981>

I. INTRODUCTION

Impinging jet injectors are commonly used in rocket engines among which the like-on-like doublet configuration is the most prominent one for its good atomization and low manufacturing cost. For example, the F-1 engine, which is the main propulsion workhorse in the Apollo lunar-landing project, employed impinging jet injectors in both the main combustion chamber and gas generator.¹ In addition, the impinging jet injector also has a wide range of applications in micro-reactors for synthesizing nanoparticles,² microfluidic chips for rapid fabrication of emulsion and suspension of biomaterials,³ and microsystems for pharma technology.⁴

Heidmann *et al.*⁵ identified three regimes for impinging liquid jets: the first regime without droplet formation, the second regime of the periodic breakup of the sheet rim, and a fragmented regime at higher jet velocities with the sheet being cut in the periodic transverse strip. For the like-on-like jet impingement, only the dynamic head of the liquid jets is exploited to destabilize the opposing streams, and the resultant sheet destabilizes and disintegrates into a cloud of droplets under the influence of inertial, surface-tension, viscous, and

aerodynamic forces.⁶ Therefore, two governing non-dimensional parameters for the atomization of perfectly aligned jet impingement are identified to be the Weber number, We , which measures the relative importance of the jet inertia compared to the surface tension, and the Reynolds number, Re , which denotes the competition between the inertial force and viscous force.^{7–12} Other than We and Re , the length-to-diameter ratio of the orifice,¹³ the pre-impingement length-to-diameter ratio,^{14,15} the impingement angle between the two impacting jets,^{6,16} the jet inflow condition,^{13,17} the ambient gas pressures,^{18,19} and the non-Newtonian effect^{20,21} were also found to significantly influence the outcome of impinging jets atomization.

Among the efforts on the impinging jet atomization, a majority of the efforts has been devoted to perfectly aligned impingement.²² Theoretical analysis and experimental measurements concerning the shape pattern,^{6,10,14} thickness,^{23,24} and velocity distribution²⁵ of the liquid sheet as well as the droplet size distribution as a result of the sheet disintegration^{6,10,26} have already shed some light upon the overall characteristics of the perfectly aligned impinging jets. As indicated by the experiment observations, there are two main instability mechanisms dictating the ligament fragmentation and droplet

formation, namely, the impact wave and aerodynamic wave.^{5,6,27,28} The impact wave, which is considered to dominate the sheet disintegration under turbulent and intermediate to high speed laminar jet, appears from the impingement point. Subsequently, the fluctuations result from the impact wave will be amplified by the aerodynamic wave until rupture of the sheet occurs, which will be followed by ligament fragmentation and droplets detaching.

In an attempt to reveal the dynamics of the instability waves, which dominate the atomization of impinging jets in such a complex multiscale two-phase flow system, numerical simulation has recently become an attractive choice. Inoue *et al.*²⁹ numerically studied the atomization process of the impinging jets by using an improved level-set method; nevertheless, their grid is insufficient to resolve the ligaments and droplets during the atomization process. Arienti *et al.*³⁰ proposed a combined level-set and Volume-of-Fluid (VOF) method coupled with the Lagrangian simulation using a dynamically adaptive grid to alleviate the computational cost. Recently, an improved adaptive mesh refinement approach (AMR) augmented VOF method by Chen *et al.*^{31,32} was exploited to address the dynamics of the liquid sheet formed by two identically impinging jets and the process of the droplet collisions. Following a similar numerical methodology, Sanjay and Das⁷ studied the influence of various factors on liquid chain formation under relatively low We numbers and Zhang *et al.*¹⁹ discussed the influence of ambient pressure on the liquid sheet disintegration and droplet formation under high We numbers.

Although extensive investigations have been conducted regarding the liquid sheet and droplet formation by the perfectly aligned jet impingement, it is worthy to note that the knowledge of the effect of misaligned impinging is determinant in atomizer design. On the one hand, for practical impinging jet injectors, the manufacturing and assembly processes would inevitably cause misalignment to a certain degree. The deviation of jet impingement caused by a large degree of misalignment would substantially influence the transfer between kinetic energy and surface energy, which alters the jet atomization and subsequent combustion performance. On the other hand, spatial dispersion of the liquid droplets and propellant mixture across the combustion chamber under misaligned jet impingement will also differ from those under its perfectly aligned counterpart. The resultant asymmetric mass distribution was found to be favorable to suppress the first tangential instability mode in rocket engines.³³

Given these complex outcomes of misaligned impinging jets, Gadgil and Raghunandan³⁴ conducted an experimental study on the misalignment effect under Re ranging from 9000 to 30 000 in which the droplet size information was collected at a single site 50 mm downstream the impingement point. The results show that as the misalignment ratio \hat{e} (ratio between the misalignment distance and the jet diameter) increases, the liquid sheet elongates while the droplet size diminishes. Pan *et al.*¹⁵ experimentally observed that the misaligned impinging jets produced larger sheet breakup length in the closed-rim regime while anticipated breakup in the open-rim regime. However, in terms of the mean droplet size, such misalignment led to systematic decreases in both regimes. To aid the practical design of impinging jet injectors, a reliability study on misalignment was carried out by Subedi *et al.*¹⁶ and they concluded that a large misalignment ratio results in small droplet sizes at the center of the liquid sheet while large droplet sizes toward the edge of the sheet.

Although experimental studies have been performed to explore the effect of colliding misalignment on the atomization of impinging jets, the fundamental understanding of the complicated instability mechanisms, the characteristics of liquid sheet disintegration, and droplet formation have not been well addressed. To this end, the present work is dedicated to revealing the characteristics of impinging jets atomization under misalignment conditions via numerical simulation. The open source code Gerris³⁵ is employed to perform the simulations, which is based on an improved VOF method with a piecewise linear interface construction augmented with the AMR technique. This paper is organized as follows: The mathematical model and numerical framework are introduced in Sec. II followed by experimental validation and grid convergence study. Afterward, the characteristics of liquid sheet disintegration and its associated instability mechanism under both perfectly and misaligned impingement will be discussed. The ensuing atomization outcomes are examined systematically under a wide range of misaligned ratios in Sec. III. Finally, the concluding remarks are summarized in Sec. IV.

II. NUMERICAL METHODOLOGY AND VALIDATION

A. Numerical method

The present numerical simulation adopts the VOF method,³⁶ which has been implemented in the open source code, Gerris.^{35,37} The formulation of the present simulation is based on three-dimensional conservation equations for incompressible, variable-density flow with viscous and surface tension forces, which can be expressed as follows:

$$\partial_t \rho + \nabla \cdot (\rho \mathbf{u}) = 0, \quad (1)$$

$$\rho(\partial_t \mathbf{u} + \mathbf{u} \cdot \nabla \mathbf{u}) = -\nabla p + \nabla \cdot (2\mu \mathbf{D}) + \sigma \kappa \delta_s \mathbf{n}, \quad (2)$$

$$\nabla \cdot \mathbf{u} = 0, \quad (3)$$

where \mathbf{u} is the velocity vector, ρ is the density, p is the pressure, μ is the dynamic viscosity, and \mathbf{D} is the deformation tensor defined as $D_{ij} = (\partial_i u_j + \partial_j u_i)/2$. In the surface tension term $\sigma \kappa \delta_s \mathbf{n}$, σ denotes the surface tensor coefficient, δ_s is a Dirac delta function, indicating that the surface tension is only concentrated near the interface, κ is the local curvature, and \mathbf{n} is the unit outward normal to the interface.

The simulation adopts the VOF method in which a VOF function $c(\mathbf{x}, t)$ is introduced to trace the two-phase interface. It is defined as the volume fraction of a given phase in each cell of the computational mesh. Subsequently, the density and viscosity can be expressed as

$$\rho(\tilde{c}) = \tilde{c} \rho_l + (1 - \tilde{c}) \rho_g, \quad (4)$$

$$\mu(\tilde{c}) = \tilde{c} \mu_l + (1 - \tilde{c}) \mu_g, \quad (5)$$

with ρ_l , ρ_g and μ_l , μ_g being the densities and viscosities of the liquid and gas phases, respectively. The field variable \tilde{c} is either identical to c or is constructed by applying spatially smoothing to c . For high-density ratio flow as concerned in the present work, the liquid-gas system property change across the interface may lead to strong shear at the interface and impair the numerical stability. Thus, the smooth filter is constructed by averaging the eight (in three-dimensional simulation) cell-corner values of c obtained by bilinear interpolation from the cell-centered values. Improved results have been obtained by this spatial filtering to density and viscosity while the associated smearing effect is limited to three discretization cells.³⁷

According to mass conservation, the advection equation for density takes the following form in terms of the volume fraction:

$$\partial_t c + \nabla \cdot (cu) = 0. \tag{6}$$

A second-order accurate time discretization of the momentum and continuity equations with the time splitting algorithm as proposed by Chorin,³⁸ whereby an unconditional stable corrector-predictor temporal scheme is adopted. A multigrid solver is employed to solve the resulting pressure-velocity coupled Laplace equation. The advection term in the momentum equation is calculated using the Bell–Colella–Glaz second-order upwind scheme,³⁹ which requires the restriction to be imposed onto the time step. Following Popinet,³⁷ the time step has been determined to satisfy Courant–Friedrich–Lewy (CFL) number less than unity (actually 0.25 is used in the present work).

The corresponding finite volume spatial discretization of the domain is undertaken using an octree-based structured hierarchical grid system, locally refined near the interface. All variables are collated at the cell centers and are interpreted as volume-averaged values for each cell. A piecewise-linear geometrical VOF method is exploited to solve the advection equation of the volume fraction.^{22,37} Moreover, a combination of the height-function curvature estimation and a well-balanced scheme for the calculation of the surface tension force is also employed. These numerical schemes have been implemented in the open source code, Gerris,³⁵ and has also been widely validated for various multiphase flow problems.^{40,41}

B. Numerical specification

Figure 1 demonstrates a schematic of the impinging jets and various geometric notations. The parent jets are issued from the injector with a straight cylindrical nozzle orifice of diameter D_j . The liquid sheet is formed by the collision of the two identical jets impacting at an impingement angle 2α . The distance between the nozzle orifice and the impinging point L_j is defined as the pre-impingement length. The symbol r denotes the radial distance from the impingement point to the edge of the liquid sheet, which is usually used to describe the position information. θ is the azimuthal angle in the jet development direction as $\theta = 180^\circ$ referring to the jet development direction while $\theta = 0^\circ$ to its opposite direction.

Generally, the jet dynamics and subsequent atomization process can be characterized by two dimensionless numbers: Weber number

$We = \rho u_j^2 D_j / \sigma$ and Reynolds number $Re = \rho u_j D_j / \mu$. It is assumed that the nozzle diameter is the same as the jet diameter when cavitation in the nozzle internal flow is negligible.¹⁹ To quantify the effect of misalignment of jets impinging, another dimensionless variable, the misalignment ratio $\hat{e} = e/D_j$, is designated to the ratio of the distance between the centerlines of two jets and the orifice diameter. By definition, when $\hat{e} = 0$ the two jets are aligned perfectly, and when $0 < \hat{e} < 1$, the misaligned impingement occurs. The computational domain is illustrated in Fig. 2(a), and its size is set to be $120D_j \times 30D_j \times 30D_j$ in x , y , and z directions, respectively, to eliminate the influence of the boundaries. Standard outflow condition is specified to the domain boundaries. Regarding the jet inflow, its velocity profile is set to be parabolic when $Re < 4000$ and $1/7$ power law when $Re > 4000$ by following Sanjay *et al.*⁷ As formulated in the present work, the Ohnesorge number $Oh = \mu_l / \sqrt{\rho_l \sigma_l D_0}$ can be expressed as a combination of We and Re numbers as $Oh = \sqrt{We}/Re$. Consequently, the present problem can be completely controlled by the three parameters, We , Re , and \hat{e} for a given set of ρ_g/ρ_l and μ_g/μ_l .

During the simulation, the grid is adaptively refined using several refinement criteria simultaneously, depending on the physical conditions, to ensure numerical accuracy and robustness. Based on the study of refinement guidelines by Chen *et al.*³¹ and Zhang *et al.*,¹⁹ the current simulation considers both value-based and gradient-based grid refinements. As shown in Fig. 2(b), the value-based refinement can ensure that the smallest grids are clustered around the liquid–gas interface to capture the complex flow structures, and the gradient-based refinement enables the VOF function to be sufficiently refined where large gradient occurs, thereby avoiding unnecessary grid refinement in the smooth flow area.

C. Numerical validation and grid convergence study

Numerical validation of the current simulation framework is conducted by comparing the formation of liquid sheet and atomization process of impinging jets against the experimental data of Ryan *et al.*¹³ In the experiment campaign, the jet impingement angle 2α is set to 60° . The nozzle diameter D_j and flow velocity U_j at the nozzle exit are 6.35×10^{-4} m and 18.5 m/s, respectively. The density and dynamic viscosity of the liquid jet are $\rho_l = 998.9$ kg/m³ and $\mu_l = 1.085 \times 10^{-5}$ Pa · s. The surrounding air medium is initially stagnant with density $\rho_g = 1.169$ kg/m³ and dynamic viscosity $\mu_g = 1.84 \times 10^{-5}$ Pa · s. Accordingly, the Re and We numbers of the jet are 11 724 and 2987, respectively. It is noteworthy that Anderson *et al.*⁴² observed that the variations in the pre-impingement length L_j from 2.5 to 38 mm had marginal effect on the liquid sheet’s breakup length and mean droplet diameter under high jet velocity. Furthermore, Heidmann *et al.*⁵ also found that the effect of the pre-impingement length on the surface waves’ dynamics can be negligible as the L_j was in between $6D_j$ and $60D_j$. Therefore, to alleviate the computational cost, the pre-impingement length L_j was set to $6D_j$ in the present work.

The resolution of the grid with refinement level N in each direction is 2^N according to the octree spatial discretization. In order to reduce the computational cost, the grid refinement level of the liquid phase is one level lower than the liquid–gas interface, and the grid level of the gaseous medium is set to 4, which is relatively coarse. A combination of parameters (N_g, N_l, N_i) is used to represent the grid levels at the gas, liquid, and gas–liquid interfaces to accommodate various

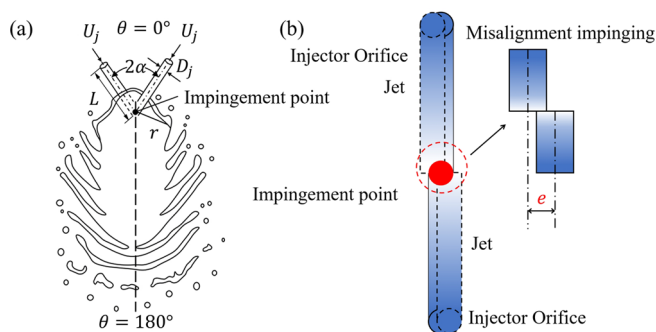


FIG. 1. Schematic of the impinging jets in (a) side view and (b) top view.

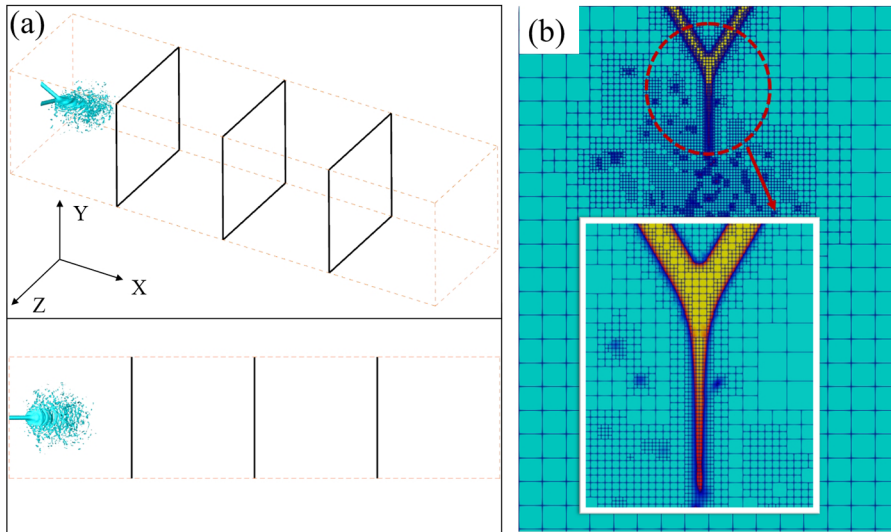


FIG. 2. (a) Schematic of the computational domain and (b) showcase of the grid refinement near the impingement point.

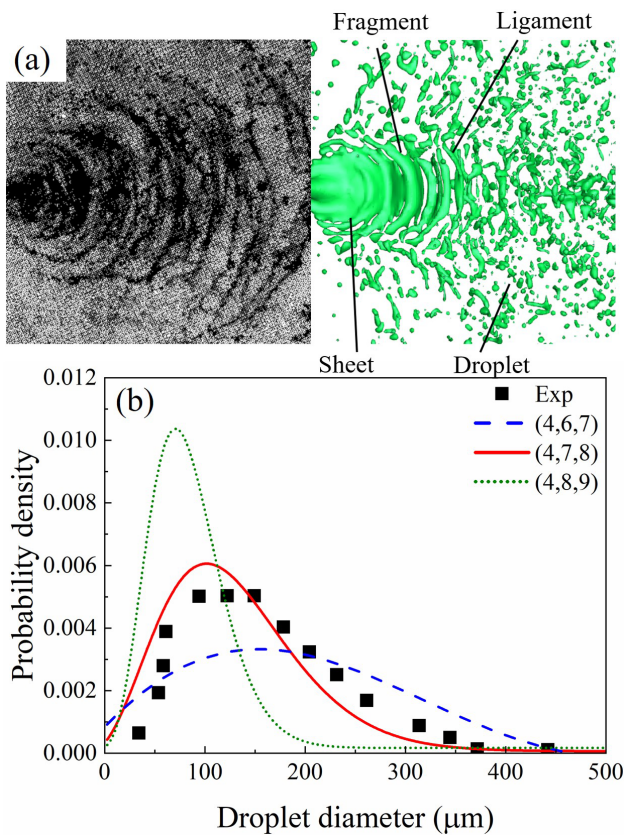


FIG. 3. Comparison of (a) detailed flow structures in impinging jets with grid refinement combination of (4, 7, 8) and (b) droplet size probability density function (PDF) $21D_j$ downstream the impingement point between the experimental data and numerical simulations.

physical scales in different flow areas. In the baseline simulation, grid refinement combination (4, 7, 8) is employed, while another two combinations (4, 6, 7) and (4, 8, 9) are implemented for grid convergence study.

In Fig. 3(a), it can be observed that with the mesh refinement parameter combination of (4, 7, 8), the numerical simulation can well resolve the detailed flow structures, including the wavy liquid sheet, fragments, ligaments, and poly-dispersed small droplets. For a quantitative comparison, the statistical probability density function (PDF) of the droplet diameters at the location $21D_j$ downstream the impingement point is collected and compared against the experiment data in Fig. 3(b). The predicted droplet size distribution is in good agreement with the experimental data with the medium grid refinement combination (4, 7, 8). For the low-resolution case, the most probable droplet

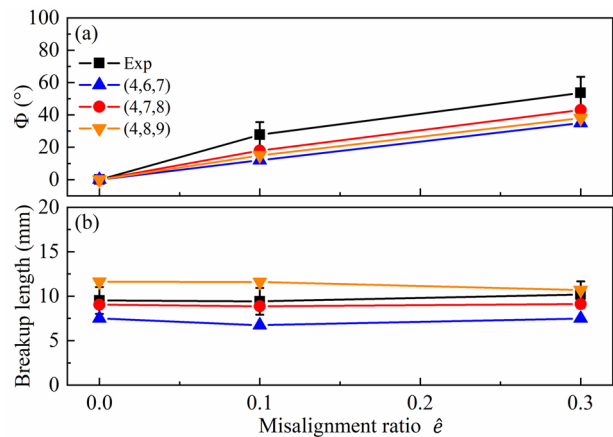


FIG. 4. Comparison of (a) sheet deflection angle and (b) sheet breakup length between experimental data and present simulations.

diameter is $150\ \mu\text{m}$, while the experimental data show a plateau from 100 to $156\ \mu\text{m}$, which can be explained that the grid is too coarse to capture the complex flow structures. With the highest grid refinement, the peak value of the PDF distribution decays toward smaller sizes.

It is worth noting that VOF simulation is exceptionally sensitive to the grid resolution. It is apparent that a too coarse grid size could lead to under-resolved fluid dynamics; however, using a refined grid size even smaller than that required for the actual physics either does not guarantee negligible numerical error. As such, Pairetti *et al.*⁴³

argued that for VOF simulation, it is more reliable to determine the desired grid resolution by the characteristic length scales relevant to the associated physical problems.

Specifically, for impinging jet atomization, the most important characteristic length scale is the liquid sheet thickness, since its deformation and subsequent fragmentation directly control the subsequent atomization outcome. This thickness of an undistorted liquid sheet before its disintegration can be evaluated following Hasson and Peck's formulation:²⁴

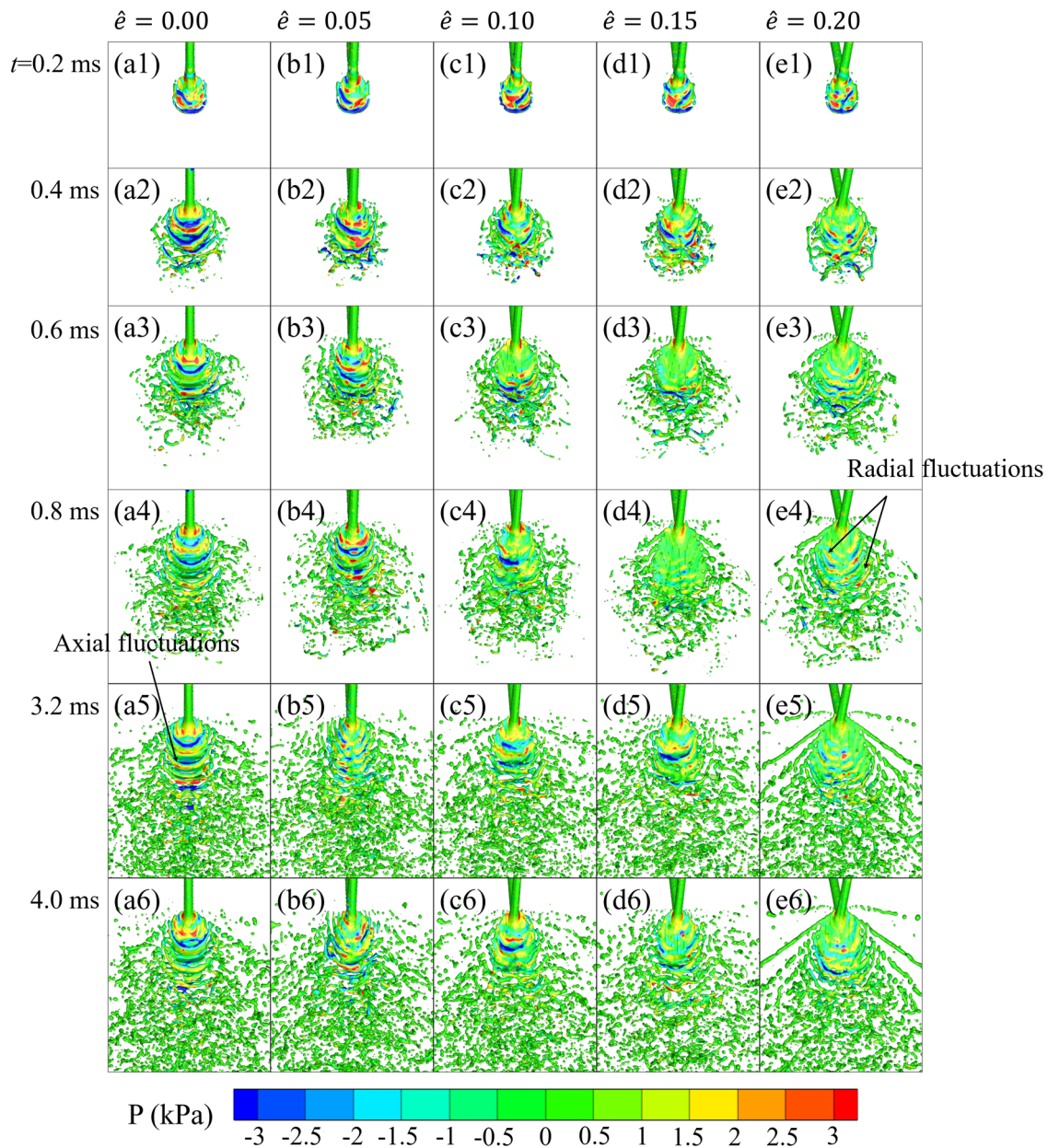


FIG. 5. Temporal evolution of the liquid sheet and its associated pressure distribution under various misalignment ratios $\hat{\epsilon}$.

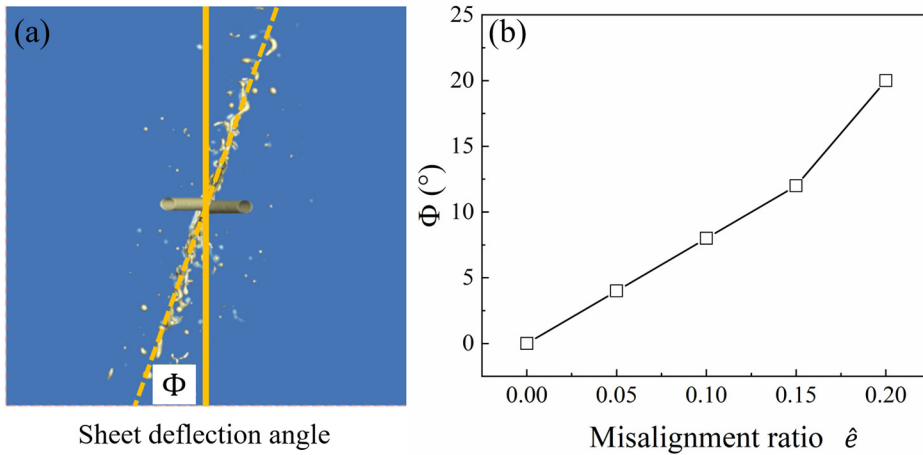


FIG. 6. (a) Illustration of the liquid sheet deflection angle and (b) the variation of the liquid sheet deflection angle with the misalignment ratio \hat{e} .

$$\frac{hr}{D_j^2} = \frac{\sin^3 \alpha}{4(1 + \cos \theta \cos \alpha)^2}, \quad (7)$$

where h is the sheet thickness, r is the radial distance, θ is the angular position, D_j is the jet diameter, and α is the impingement half angle, as denoted in Fig. 1. For $2\alpha = 60^\circ$ in the present work, the sheet thickness reaches its maximum value of $hr/D_j^2 = 1.74$ in the streamwise direction. Chen *et al.*³¹ found that the liquid sheet dynamics cannot be adequately resolved if the sheet thickness is covered by no more than two grid cells, suggesting a condition for the minimum grid size as $\Delta x_{min} < 0.5h$. Together with Hasson and Peck's formulation, the grid size requirement for resolving the sheet can be derived as $\Delta x_{min}/D_j < 0.87/(r/D_j)$. Accordingly, the grid levels of 7, 8, and 9 are sufficient to resolve the liquid sheet disintegration at radial distances shorter than $3.71D_j$, $7.43D_j$, and $14.85D_j$, respectively. In the present study, since the sheet breakup length at $We = 2987$ is predicted to be $(6.27 \pm 0.3)D_j$,¹⁹ we thereby adopted the refinement level 8 as the most physically relevant one to reproduce the liquid sheet dynamics at the present operating condition. Moreover, the dimensional grid size corresponding to refinement level 8 is $74 \mu\text{m}$, which is also comparable to the recommended minimum grid size over the range of $50\text{--}70 \mu\text{m}$ in a previous simulation of a similar problem using Gerris solver.¹⁹

To further verify the current grid refinement for liquid jet impingement under the misalignment effect, we have conducted a new simulation with three different refinement combinations and validated against the experiment of Subedi *et al.*¹⁶ For experimental configuration, the water liquid jets were ejected from orifices of diameter $D_j = 1.2 \text{ mm}$ and impinged upon each other in the atmospheric air, with $We = 1345$ and $Re = 10\,000$. From Figs. 4(a) and 4(b), the predicted sheet deflection angle ϕ and the breakup length agree well with the experiment with the grid refinement (4, 7, 8), which is consistent with the physical scale resolution $D_j/\Delta x_{min}$ predicted from Ryan's experiment.¹³ As for the sheet deflection angle ϕ , it is less sensitive to the grid refinement under a wide range of misalignment ratios, as can be observed in Fig. 4(a). Furthermore, Fig. 4(b) shows that the poor grid resolution of (4, 6, 7) causes an underestimation of the sheet breakup length because the parallel interfaces of a thin liquid sheet

tend to merge early with the sheet thickness resolved by a single large grid cell, which then triggers the sheet fragmentation; in contrast, the over-resolved grid with level (4, 8, 9) exhibits an opposite trend because multiple smaller grid cells across the sheet make it more difficult for the parallel interfaces to merge, thereby delaying the sheet

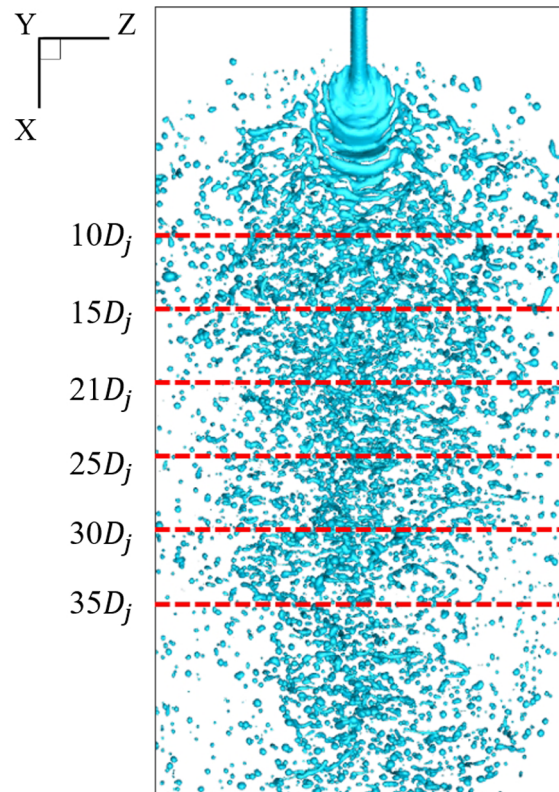


FIG. 7. Schematic diagram of the sampling planes for SMD statistics.

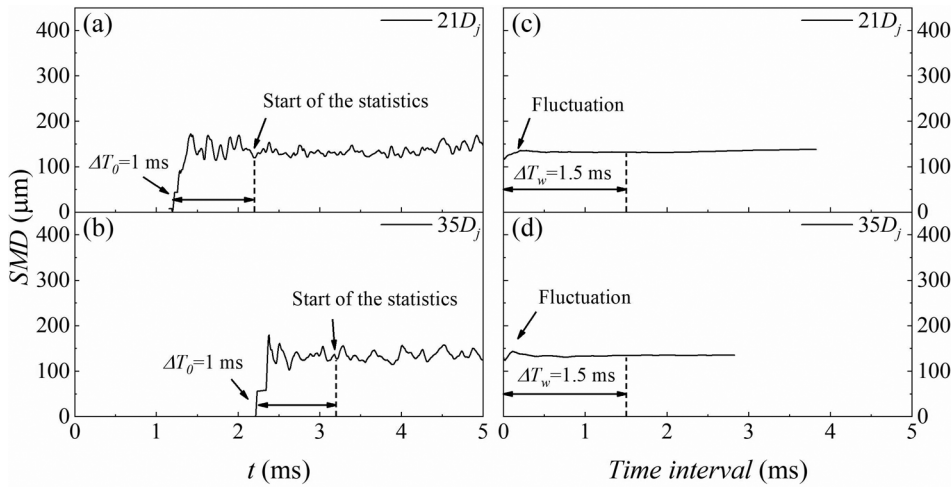


FIG. 8. Temporal evolution of the droplet SMD and the time-averaged droplet SMD with different averaging intervals at the positions [(a) and (c)] 21 D_j and [(b) and (d)] 35 D_j downstream the impingement point for misalignment ratio $\hat{e} = 0.10$.

fragmentation. These results further substantiate the selection of the refinement level (4, 7, 8) for the present simulation under misaligned impingement. Therefore, the mesh refinement combination of (4, 7, 8) is used in subsequent simulations.

III. RESULTS AND DISCUSSION

A. General characteristics of misaligned jet impingement

By following the same experiment layout of Ryan *et al.*,¹³ the impinging jets with $Re = 11\,724$ and $We = 2987$ were numerically revisited under various misalignment ratios. For perfectly aligned impinging jets as shown in Fig. 5(a-1), after colliding with each other, the liquid flows from the impingement point to the sheet periphery under inertial force. Once the liquid sheet is formed, the aerodynamic force produces rapidly growing waves either by itself or in conjunction with the impact waves as depicted in Fig. 5(a-2). Subsequently, the liquid sheet becomes unstable with an oscillating boundary; then, the sheet is torn off between the wave crests and troughs. The arc-shaped fragments detached from the unstable sheet boundary then contracted into ligaments under surface tension force, which eventually disintegrate into large droplets under the Rayleigh–Plateau instability. Since the hydrodynamic instabilities are mainly constrained to the liquid sheet, this indicates that the major portion of the ensuing atomization

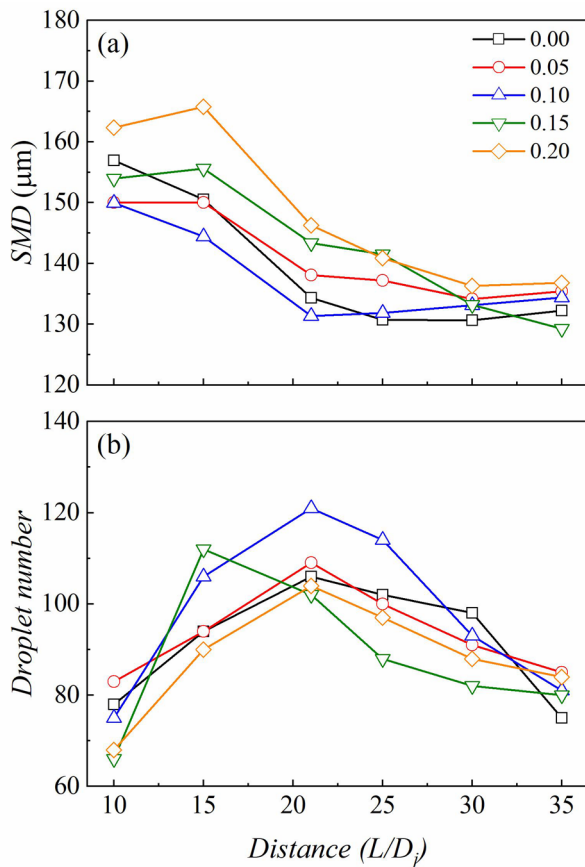


FIG. 9. (a) The droplet SMD and (b) the number of the droplets at various positions downstream the impingement point.

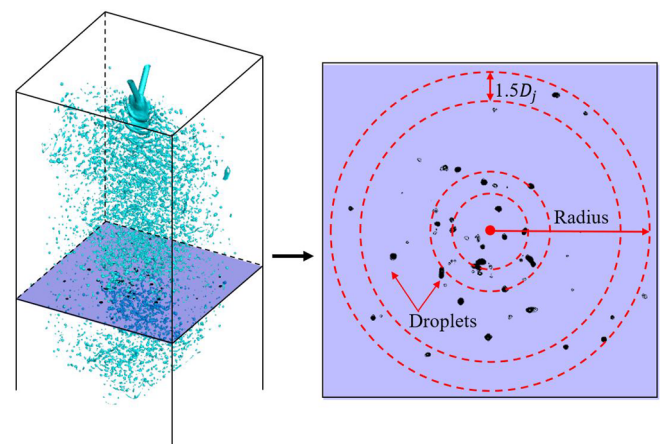


FIG. 10. Schematic diagram of the position and method used for the statistics of the spatial mass distribution.

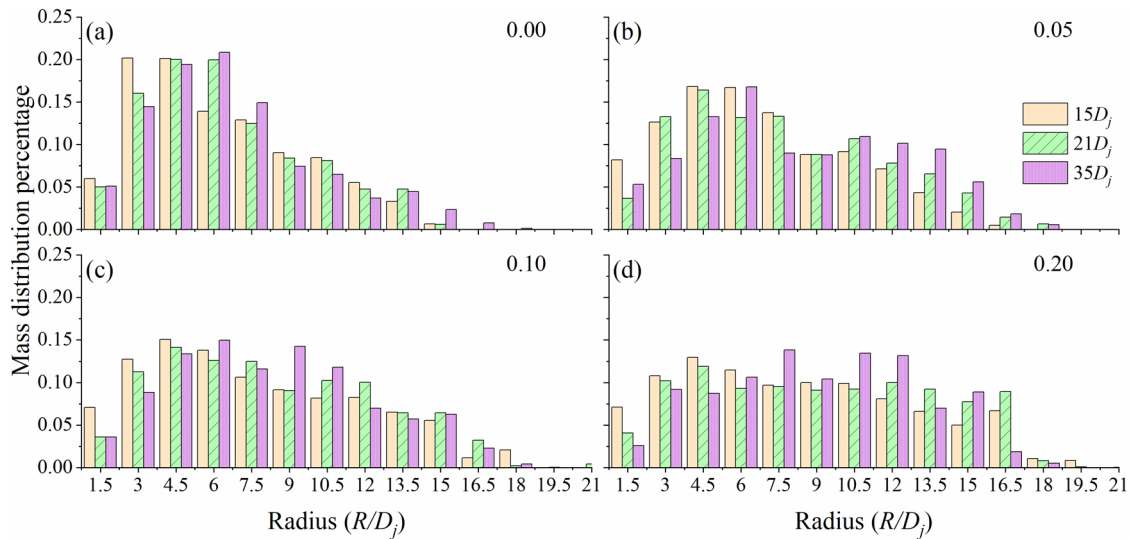


FIG. 11. The spatial mass distribution of the droplets at different positions $15D_j$, $21D_j$, $35D_j$ downstream the impingement point with different misalignment ratios for (a) $\hat{e} = 0.00$, (b) $\hat{e} = 0.05$, (c) $\hat{e} = 0.10$, and (d) $\hat{e} = 0.20$.

lies along the plane of the spray fan, and therefore, the mass distribution pattern is governed by the orientation of the liquid sheet.

Based on the initial inspection, four cases have been conducted with misalignment ratios \hat{e} of 0.05, 0.10, 0.15, and 0.20 while maintaining the same Re and We numbers ($Re = 11\,724$, $We = 2987$), respectively. It is obvious that the most fundamental difference between the perfectly aligned and misaligned impinging jets is the effective collision area of the jets. The vertical component of momentum is unaffected, whether the jets are perfectly aligned or not. In the case of perfectly aligned impinging jets, the momentum in the y -direction gets nullified, and the liquid spreads in the radial direction. However, in the misaligned case, the horizontal momentum has two different components during impingement. The part of the jet that collides with each other behaves similarly as before and tends to spread in the radial direction. The remaining part of the jet has an inert of moving forward in its original direction but immediately encounters and merges with the radially expanding liquid sheet formed upon the direct impingement, leading to the deflection of the original liquid sheet as a result of the y -direction momentum balance.

Figure 5 also demonstrates the temporal evolution of pressure field on the impinged liquid sheet. For the perfectly aligned impinging jets, the pressure is alternately distributed on the liquid sheet in the

streamwise direction as shown in Fig. 5(a-2). This is consistent with the sheet's topology, which curves the streamlines and modulates the velocity of the gaseous flow in its vicinity. As a result, remarkable pressure differences are induced at the wave crests and troughs on the sheet. The alternate distribution of high and low pressure promotes the growth of instability of the sheet and enhances the flapping amplitude until the sheet is disintegrated. As the misalignment ratio increases, the most obvious discrepancy is that the pressure peaks gradually shift from the center to the lateral sides of the liquid sheet as indicated from Figs. 5(c-2), 5(d-2), (d-5), and (e-2). Meanwhile, the amplitudes of fluctuation on both crests and troughs decline significantly as the misalignment ratio increases. The variation of liquid sheet's topology and pressure distribution shown in side view is also displayed by Fig. S1 in the supplementary material.

Before quantifying the overall characteristics of the misaligned jet impingement, the deflection angle of the liquid sheet is assessed first. The sheet deflection angle Φ indicated in Fig. 6(a) is defined as the angle between the liquid sheet of the perfectly aligned impingement and that formed by the misaligned one. Figure 6(b) shows that the deflection angle of the liquid sheet becomes larger as the impinging misalignment ratio increases. For small misalignment ratio $\hat{e} = 0.05$,

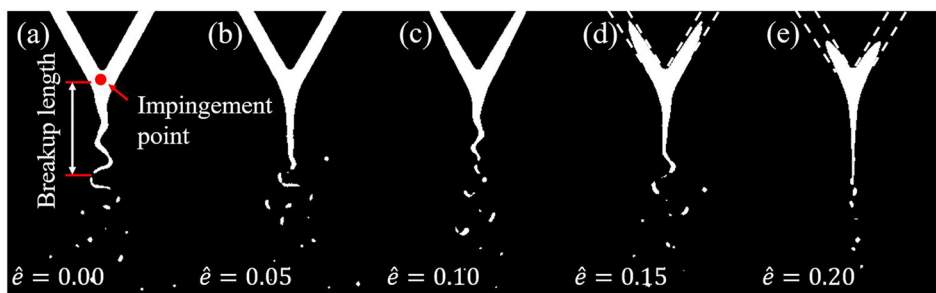


FIG. 12. Illustration of the liquid sheet breakup length with different misalignment ratios for (a) $\hat{e} = 0.00$, (b) $\hat{e} = 0.05$, (c) $\hat{e} = 0.10$, (d) $\hat{e} = 0.15$, and (e) $\hat{e} = 0.20$.

the sheet deflects 4° angle, whereas it becomes as large as 20° for $\hat{e} = 0.20$.

B. Atomization and droplet formation

The deformation and breakup of droplets are important in the spray and atomization processes,^{44,45} and for a comprehensive view of the atomization process, Fig. 7 displays the instantaneous spatial distribution of the simulated spray. The entire atomization process can be roughly divided into two stages, namely, the primary and secondary atomization. During the primary atomization, the impact waves arising from the hydrodynamic instability generate large-amplitude disturbances and cause the liquid sheet to disintegrate. Then, the arc-shaped ligaments further fragment into poly-dispersed droplets during the second atomization phase in downstream locations.

Given the importance of coalescence and breaking process of the droplet in the combustion process,^{46,47} the Sauter mean diameter (SMD, $d_{32} = \sum n_i d_i^3 / \sum n_i d_i^2$) is taken as the metric to evaluate the atomization quality. Statistics of the SMD are conducted at 6 horizontal planes downstream of the impingement point as denoted in Fig. 7. For droplet information statistics, it is essential to determine the starting instant and time interval for the sampling. Here, we adopt a *a posteriori* test on the misaligned impinging jets with the misalignment ratio $\hat{e} = 0.10$ as shown in Fig. 8. Combining the time histories of SMD at both intermediate ($21D_j$) and the farthest locations ($35D_j$), the starting instant is chosen to be $\Delta T_0 = 1.0$ ms after the appearance of the first droplet at the specified plane. Once the starting instant is determined, the statistical steady state can be achieved with a relatively large time interval $\Delta T_w = 1.5$ ms as shown in Figs. 8(c) and 8(d).

The droplet SMD at different streamwise locations under different misalignment ratios is presented in Fig. 9(a). The variations of SMD under different misalignment ratios generally follow a similar trend that it first undergoes a steep decrease and then levels off after $L > 20D_j$. The initial rapid decrease in SMD corresponds to the primary atomization phase in which disintegration of the liquid sheet is dominated by the impact waves. As the coalescence of droplets dominates the collision outcome in the secondary atomization phase,⁴⁸ the fragmentation of ligaments, which reduces the SMD, is balanced by the coalescence of poly-dispersed droplets, which increases the SMD, causing a saturation trend of SMD at downstream locations. Another prominent finding from Fig. 9(a) is that the droplet size does not change monotonously with the variation of impinging misalignment ratio. When \hat{e} equals 0.05, the droplet size is increased compared to the perfectly aligned impinging jets except at the vicinity of the impingement point. However, this tendency reverses when the misalignment ratio \hat{e} approaches 0.1 at the upstream locations ($L/D_j < 20$). As the misalignment ratio further increases, the droplet size shows a notable increase in comparison with their perfectly aligned counterpart.

Statistically, the droplet numbers at corresponding locations are also collected as shown in Fig. 9(b). Generally, the number of droplets first increases in the primary atomization phase and then decreases in the secondary atomization phase, which is consistent with the variation tendency of the droplet SMD. Specifically, with relatively small misalignment ($\hat{e} = 0.05$), the droplet number tends to exceed that of the perfect impingement case, which corresponds to reduced SMD at

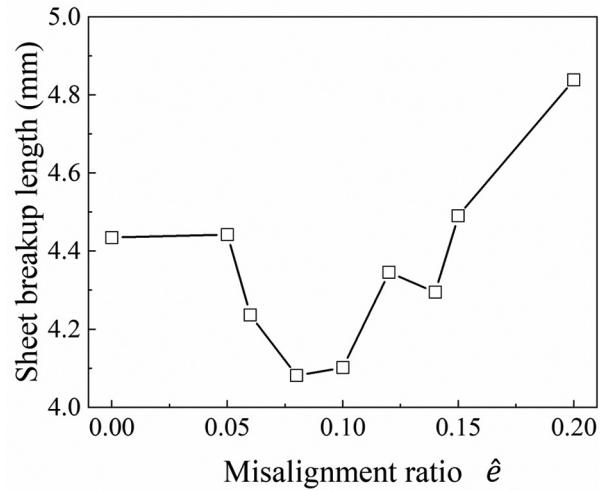


FIG. 13. The variation of the sheet breakup length with the misalignment ratio \hat{e} .

upstream locations. However, when the misalignment ratio equals 0.1, it produces a significantly larger amount of droplets than that for $\hat{e} = 0$. This explains the reduction of SMD for $\hat{e} = 0.1$ case at upstream locations, while the increasing SMD at downstream locations is likely attributed to the frequent coalescence between droplets.

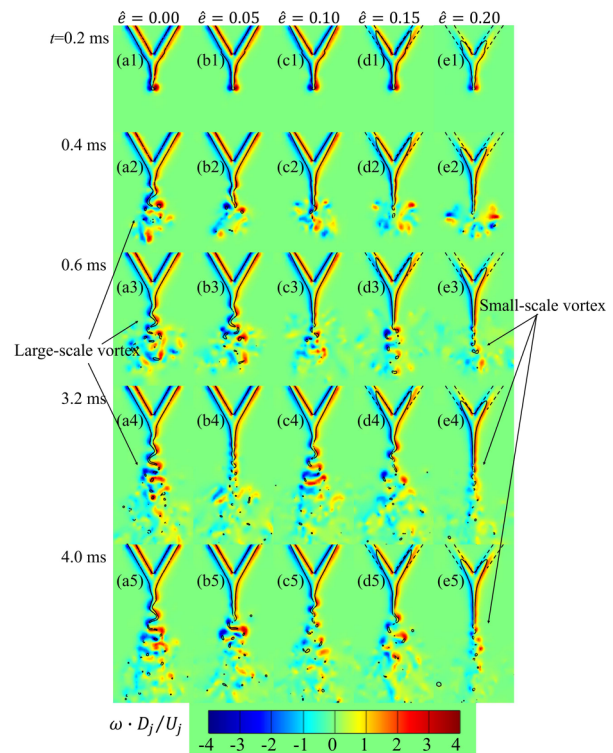


FIG. 14. Instantaneous vorticity distributions on the plane perpendicular to the liquid sheet under different misalignment ratios \hat{e} .

C. Droplet spatial distribution

To further quantify the influence of the misalignment effect on impinging jets atomization, the spatial mass distribution of droplets is estimated based on the simulation results. The spatially dispersed droplets were sampled at three cross-sections that are located at $15D_j$, $21D_j$, and $35D_j$ downstream the impingement point, respectively. A typical collection plane is schematized in Fig. 10 to illustrate how droplets are sampled at a typical cross section, where a shallow cuboid of comparable height to the jet diameter is placed to emulate the collection pattern used in the experiments of Subedi *et al.* and Gadgil *et al.* experiments.^{16,34} During the same time interval for SMD statistics, all the droplets whose centroid crosses the cuboid will be counted, and therefore, the radial distance between the centroid of each droplet and the central axis can be calculated. Afterward, the droplets' mass collected within this cuboid are divided into multiple concentric circles with an increment of $1.5D_j$ in the radial direction.

Figure 11 presents the histogram of mass distribution that is normalized by the total sampled quantity at three typical streamwise locations for different misalignment ratios. As shown in Fig. 11(a), when the perfectly aligned impinging occurs, most of the mass is concentrated in the radial range of $3.0 - 7.5D_j$ at different streamwise locations. This spatial mass distribution of the dispersed droplets is directly related to the liquid sheet disintegration, as the major portion of the liquid evolves along the plane of the liquid sheet. However,

under misaligned impinging, the radial dispersion of the atomized droplets becomes more uniform. For misalignment ratio $\hat{\epsilon} = 0.05$, as can be observed in Fig. 11(b), the mass fraction at the two downstream locations increases compared to the perfectly aligned case. As the misalignment ratio continues to increase, such as the cases $\hat{\epsilon} = 0.10$ and 0.20 , the droplet mass exhibits a more uniform spatial distribution albeit the enlarged SMD at $\hat{\epsilon} = 0.20$.

D. The governing mechanism for the liquid sheet disintegration

To scrutinize the mechanism responsible for the above atomization characteristics, we next focus on the dynamics of the liquid sheet formed upon jet impingement as it dictates the subsequent primary atomization process. The sheet breakup length, which measures the distance from the impingement point to the first breakup point on the intact liquid sheet along the centerline axis, is obtained through image gray processing. Figure 12 exhibits instantaneous gray images of the liquid phase for various misalignment ratios. Given that the breakup location may vary notably over time, the time-averaged value of the breakup length is calculated with 150 instances in the present study. The variations of breakup length with different misalignment ratios are present in Fig. 13. It can be observed that for small impinging misalignment ratio ($\hat{\epsilon} = 0.05$), change in the sheet breakup length is

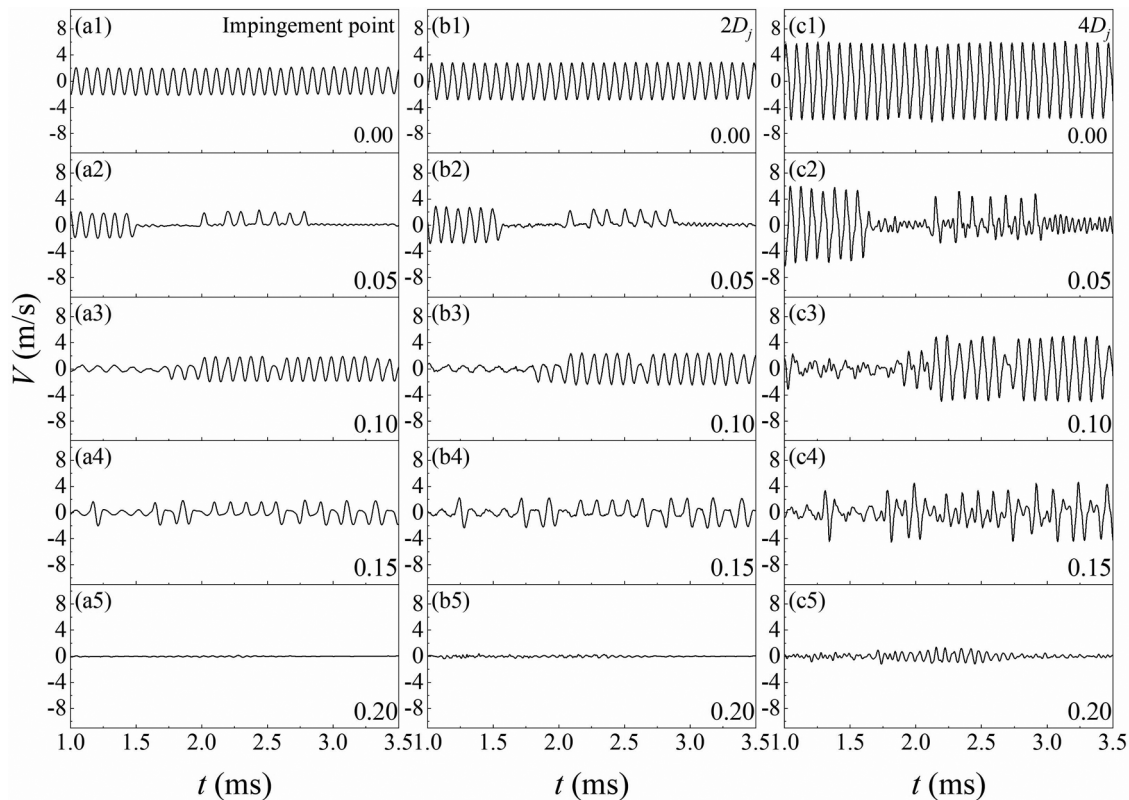


FIG. 15. The velocity fluctuations in the direction perpendicular to the liquid sheet at [(a-1)–(a-5)] impingement point, [(b-1)–(b-5)] $2D_j$ and [(c-1)–(c-5)] $4D_j$ downstream the impingement point.

negligible. However, when the misalignment ratio approaches 0.10, the sheet breakup length decreases significantly, which can be also seen in Fig. 12(c). It is interesting to find that, as the misalignment of the impinging jets increases, the sheet breakup length rises again, to even larger values than the perfectly aligned case when \hat{e} exceeds 0.15. This non-monotonic change in the sheet breakup length inspires us to further explore the underlying physics of the hydrodynamic instabilities on the liquid sheet in the misaligned scenario.

Figure 14 shows the vorticity field (ω) of the liquid sheet to further clarify the effect of the misaligned impingement. Since the liquid sheet rotates in the misaligned impinging process, it is necessary to take sheet deflection into account in vorticity calculation by choosing the direction of to be perpendicular to the liquid sheet, resulting in the normalized vorticity as $\omega \cdot D_j / u_j$. We can verify that vorticity generation is accompanied by the fluctuations of the liquid sheet. For perfectly aligned impinging jets in Figs. 14(a-1)–14(a-5), the shear effect from the relative motion between the internal flow and the surface flow of the liquid sheet free surface causes vorticity generation normal to the sheet expanding direction. The large-scale vortices staggered alongside the liquid sheet manifest drastic fluctuations of the sheet motion, which forms the sheet’s crests and troughs.

As can be observed in Figs. 14(b-3)–14(b-5), 14(c-3)–14(c-5), and 14(d-3)–14(d-5), for small-to-medium misalignment ratios $\hat{e} = 0.05, 0.10,$ and $0.15,$ the flipping mode and its associated vorticity field exhibit obvious intermittency even after the initial development stages. For example, regarding Figs. 14(b-3)–14(b-5) for $\hat{e} = 0.05,$ the sheet’s flapping intensity is significantly suppressed at $t = 3.2$ ms with reduced vorticity magnitude, whereas it resurges again later at $t = 4.0$ ms rendering the sheet’s motion and vorticity field similar to those in the early stage at $t = 0.6$ ms. However, with the largest impinging misalignment $\hat{e} = 0.20,$ the previously wavy liquid sheet becomes almost flat and the associated vortices become notably smaller. Accordingly, the disintegration of the liquid sheet is quite different from the perfectly aligned impingement in that the pinched-off droplets are less scattered downstream. This non-monotonic phenomenon suggests that partial impingement introduces a new mechanism into the instability evolution and subsequent breakup for the liquid sheet.

Dombrowski and Hooper¹⁷ suggested that for intermediate-to-high speed impinging jets, the disintegration of the liquid sheet should be attributed to the impact wave originated from the impingement point. In order to elucidate the dynamics of the impact wave, time histories of the instantaneous velocity in the direction perpendicular to

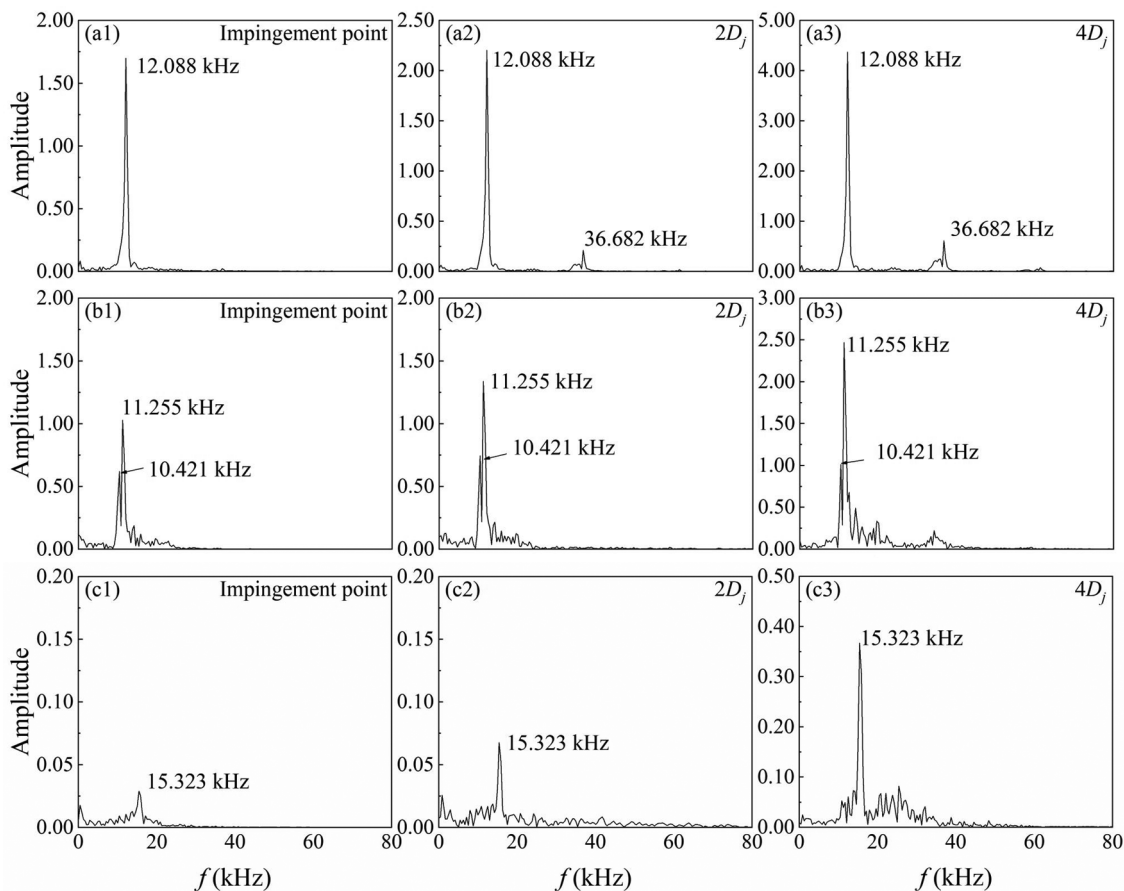


FIG. 16. Spectrum analysis of the velocity fluctuations at impingement point, $2D_j$ and $4D_j$ downstream the impingement point with different misalignment ratios [(a-1)–(a-3)] $\hat{e} = 0.00,$ [(b-1)–(b-3)] $\hat{e} = 0.10,$ and [(c-1)–(c-3)] $\hat{e} = 0.20.$

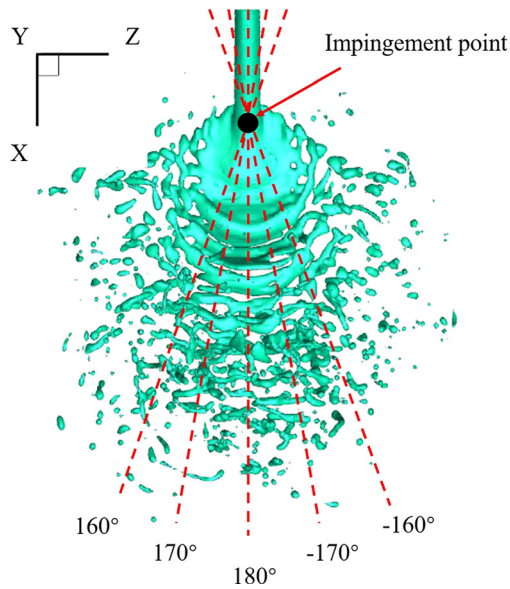


FIG. 17. Schematic diagram showcasing different angular positions.

the liquid sheet are collected at the impingement point and locations $2D_j$ and $4D_j$ downstream along the centerline, respectively. It can be seen from Fig. 15(a) that, the liquid sheet formed by the perfectly aligned impinging jets always exhibits a regular fluctuation mode. However, with a non-zero misalignment, the periodic velocity fluctuation mode is replaced by an intermittent one. Additionally, the variations of the magnitude of the velocity fluctuation embody a non-monotonic dependence on the impinging misalignment ratios. For the largest $\hat{\epsilon}$ concerned, the velocity fluctuations at both the impingement point and its downstream locations are dramatically diminished.

Spectrum analyses of the velocity fluctuations corresponding to the same spatial locations in Fig. 15 are presented in Fig. 16. It can be seen from Fig. 16(a) that, when perfectly aligned impinging occurs, a fundamental wave of frequency 12.088 kHz is resolved at the impingement point, as well as $2D_j$ and $4D_j$ downstream along the centerline. A harmonic wave with higher frequency and lower amplitude emerges at locations $2D_j$ and $4D_j$ downstream the impingement point. It is worth noting that Ryan *et al.*¹³ also measured the surface wave on the liquid sheet experimentally, yielding a wavelength of 1.5 ± 0.5 mm. With the characteristic sheet velocity being identical to the jet velocity, their fundamental wave frequency is estimated to fall in the range of 9.250 – 18.500 kHz. Given the uncertainty in measurement, the fundamental frequency predicted by the present simulation agrees well

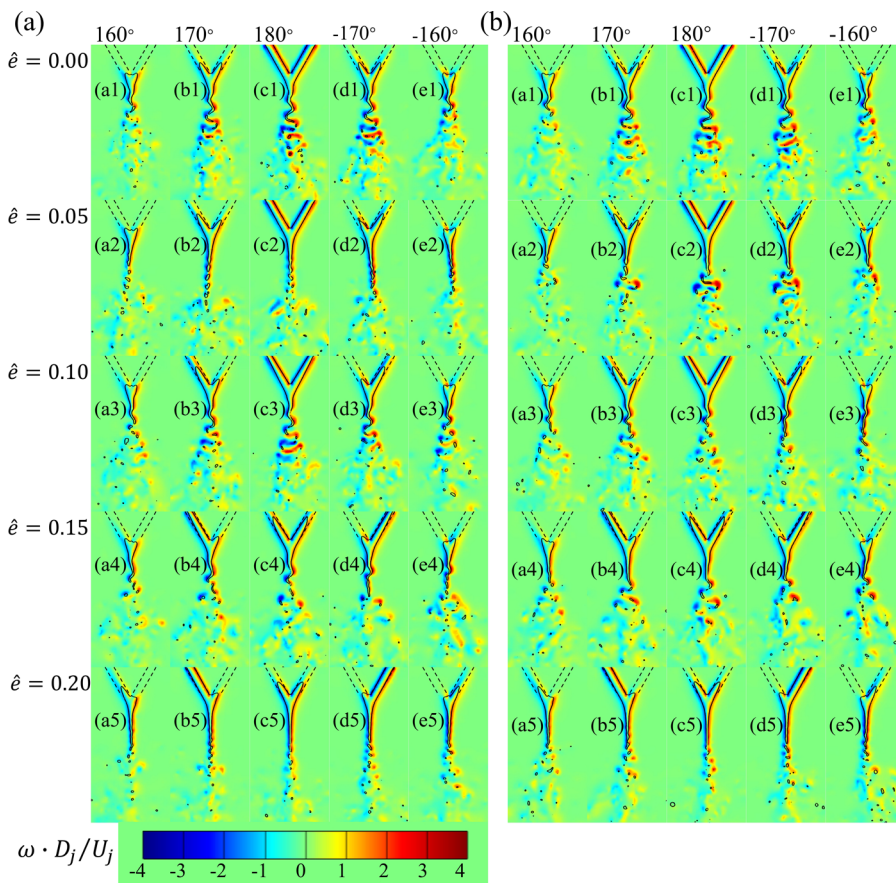


FIG. 18. The disintegration of the liquid sheet and vorticity variation at different angular positions with various misalignment ratios $\hat{\epsilon}$ at (a) $t = 3.2$ ms and (b) $t = 4.0$ ms.

with the experiment, which again substantiates the accuracy of the simulation methodology. The good agreement also confirms that the dominating instability mechanism is the impact wave, which originates from the impingement point and is further amplified downstream when coupled with external aerodynamic instability for the perfectly aligned impinging scenario.

Figure 16(b) shows a different mode of fluctuation spectrum for small misalignment ratio ($\hat{e} = 0.10$). In addition to the fundamental frequency ($f = 11.255$ kHz) caused by the impact wave, another frequency peak ($f = 10.421$ kHz) can be detected, which implies that the intrinsic instability of the perfectly aligned impinging jets is modulated by the partial impingement. As the misalignment ratio further increases, Fig. 16(c) shows that the liquid sheet fluctuates at a higher frequency ($f = 15.323$ kHz) but less energetic mode compared to the perfectly impinging case. This can be understood that with a large misalignment ratio the effective impact is minimized by the lateral stretch effect, which generates a smaller-size wave structure, thereby increasing the wave frequency while decreasing the wave amplitude. Since the flapping amplitude of the liquid sheet is notably declined for large misalignment ratios, it is natural to expect that the liquid sheet becomes more stable, which explains the increasing breakup length with \hat{e} in Fig. 13.

The distinctive liquid sheet dynamics and disintegration for misaligned impinging are likely caused by a lateral stretch effect, which is associated with the additional momentum supplied to the liquid sheet by the lateral jet portions that are not engaged in the head-on impingement. For further demonstration, we inspect several cross sections of the liquid sheet with different angular positions as schematized in Fig. 17. Subsequently, Fig. 18 plots the calculated vorticity field at these cross sections for two different

instants, 3.2 and 4.0 ms. For none ($\hat{e} = 0$) and low impinging ($\hat{e} = 0.05$) misalignment ratios in Figs. 18(a-1)–18(e-1) and 18(a-2)–18(e-2), the vorticity field on the central plane ($\theta = 180^\circ$) dominates the evolution of the liquid sheet. However, as the misalignment ratio further increases, the lateral stretch effect becomes more pronounced, with the vorticity fields at the angular position $|\theta| = 170^\circ$ dominating over the ones at the central plane.

This lateral stretch effect is anticipated to stimulate the hydrodynamic instability at other angular positions instead of the central plane, as illustrated by the velocity fluctuations at various angular positions in Fig. 19. Nearly periodic fluctuations occur at different angular positions, and their mean values are all around zero in the case of perfectly aligned impinging jets in Fig. 19(a). However, for a large degree of misalignment ($\hat{e} = 0.20$), the fluctuations at different angular positions show a clear disparity. In the central plane, the velocity fluctuation magnitude is relatively small, whereas it increases as the angular position switches from central to lateral. Another finding on the sheet fluctuation at different angular positions is that the time-averaged velocity no longer fluctuates around zero for $\hat{e} = 0.20$, which indicates a rotation of the liquid sheet.

E. Further discussion on the misalignment effect

So far, we have analyzed the misalignment effect of the impinging jets on modulating the hydrodynamic instability and disintegration process of the liquid sheet. The non-monotonic influence of the impinging misalignment on the ensuing atomization performance and droplet spatial distribution is inherently related to the competition between the liquid sheet disintegration dominated by the impact wave and the spatial dispersion induced by the lateral stretch effect.

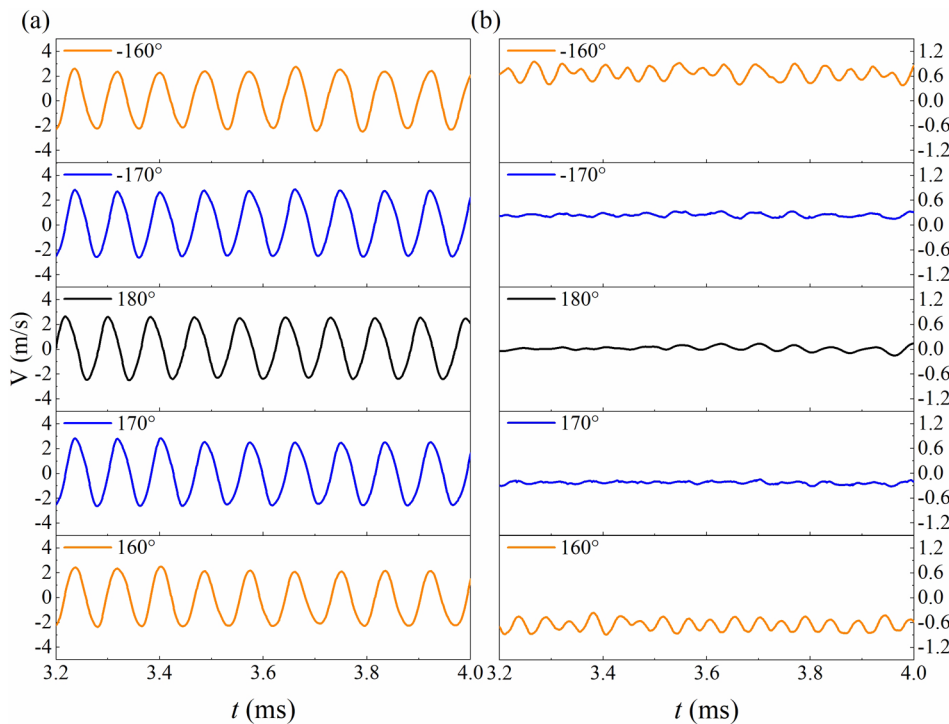


FIG. 19. Velocity fluctuations perpendicular to the direction of the liquid sheet at $2D_j$ downstream the impingement point for (a) perfectly colliding $\hat{e} = 0$ and (b) misalignment colliding with misalignment ratio $\hat{e} = 0.20$.

Specifically, the decreasing SMD for the intermediate misalignment ratio ($\hat{\epsilon} = 0.1$) should result from the lateral stretching, which induces a larger fluctuation of liquid sheet and thereby a stronger breakup effect during the formation of the primary spray. In contrast, at the large misalignment ratio ($\hat{\epsilon} = 0.20$), the lateral stretching dominates over the impact waves, which causes a suppressed sheet fluctuation and consequently leads to weaker atomization, as reflected by the significant increase in SMD and decrease in droplet number in Fig. 9. This non-monotonic variation of the droplet SMD is also consistent with the dynamical behaviors of the liquid sheet, especially its breakup length as in Fig. 13, which implies that the droplet size in the near field is dominated by the primary atomization process. Moreover, the lateral stretching induced by misaligned impingement also yields a more uniform spatial distribution in the combustion chamber as discussed in Sec. III C, thereby enabling an enhanced mixing between propellants via the proper orientation of the impinging jet pairs. This result has a promising implication that the misalignment ratio could serve as a control parameter in future injector design for optimized atomization characteristics.

IV. CONCLUDING REMARKS

In this paper, an improved VOF method with an adaptive mesh refinement algorithm was adopted to study the atomization characteristics of misaligned impinging jets and the governing mechanism for the liquid sheet disintegration. Phenomenologically, it was found that the misalignment alters the topology of the liquid sheet formed upon the jet impingement, as the pressure peak gradually shifts from the center to the lateral sides while the pressure fluctuations decline remarkably. The atomization outcome was that the spray SMD shows a non-monotonic dependence on the impinging misalignment ratio $\hat{\epsilon}$, indicating that the best atomization is achieved with $\hat{\epsilon} = 0.1$ under operating conditions concerned in the present work. Furthermore, based on the statistics of the droplet mass distribution, the improved spray performance under moderately misaligned impingement is also manifest in the more uniformly dispersed droplets throughout the chamber downstream.

The non-monotonic dependence of the atomization outcomes on the impinging misalignment ratio can be attributed to the instability and disintegration of the liquid sheet. This is evident from the non-monotonic dependence of the liquid sheet breakup length on $\hat{\epsilon}$ that it first decreases with $\hat{\epsilon}$ when $\hat{\epsilon} < 0.1$ and then increases with $\hat{\epsilon}$ when $\hat{\epsilon} > 0.1$. Further analyses of the vorticity data and velocity fluctuations revealed that the involvement of a lateral stretch effect is responsible for the distinct breakup behavior of the liquid sheet under misaligned impingement. Specifically, it intensifies the vorticity production on the lateral side of the liquid sheet and hence promotes the intrinsic hydrodynamic instability for small-to-moderate $\hat{\epsilon}$. However, for larger $\hat{\epsilon}$, the lateral stretch effect dominates over the initial impact wave in the liquid sheet disintegration, causing the emergence of a higher-frequency but less-energetic mode. These findings inspire us to consider the misalignment ratio as a tuning parameter for desired atomization characteristics in future injector design and propellant mixing control.

SUPPLEMENTARY MATERIAL

See the [supplementary material](#) for the temporal evolution of the liquid sheet and its associated pressure distribution under various misalignment ratio $\hat{\epsilon}$ from a side view.

ACKNOWLEDGMENTS

This work was supported by the National Natural Science Foundation of China (Grant Nos. 12072194 and 51806013), the foundation research funds of Ministry of Industry and Information Technology (Grant Nos. JCKY2019602D018 and WDZC-2019-JGKK-02), the Beijing Institute of Technology Research Fund Program for Young Scholars (Grant No. 2020CX04047), and partly by the Shanghai Sailing Program (Grant No. 20YF1420600). The authors are grateful to Dr. Chengming He for his insightful advice for the numerical simulation.

DATA AVAILABILITY

The data that support the findings of this study are available from the corresponding author upon reasonable request.

REFERENCES

- J. C. Oefelein and V. Yang, "Comprehensive review of liquid-propellant combustion instabilities in F-1 engines," *J. Propul. Power* **9**, 657 (1993).
- R. Baber, L. Mazzei, N. T. K. Thanh, and A. Gavrilidis, "Synthesis of silver nanoparticles using a microfluidic impinging jet reactor," *J. Flow Chem.* **6**, 268 (2016).
- C. W. Visser, T. Kamperman, L. P. Karbaat, D. Lohse, and M. Karperien, "In-air microfluidics enables rapid fabrication of emulsions, suspensions, and 3D modular (bio) materials," *Sci. Adv.* **4**, eaao1175 (2018).
- A. Dietzel, *Microsystems for Pharmatechnology: Manipulation of Fluids, Particles, Droplets, and Cells* (Springer, Heidelberg, 2016).
- M. F. Heidmann, R. J. Priem, and J. C. Humphrey, "A study of sprays formed by two impinging jets," NACA TN **3835** (1957).
- N. Bremond and E. Villermaux, "Atomization by jet impact," *J. Fluid Mech.* **549**, 273 (2006).
- V. Sanjay and A. K. Das, "Formation of liquid chain by collision of two laminar jets," *Phys. Fluids* **29**, 112101 (2017).
- E. A. Ibrahim and A. J. Przekwas, "Impinging jets atomization," *Phys. Fluids A* **3**, 2981 (1991).
- N. Ashgriz, W. Brocklehurst, and D. Talley, "Mixing mechanisms in a pair of impinging jets," *J. Propul. Power* **17**, 736 (2001).
- J. W. M. Bush and A. E. Hasha, "On the collision of laminar jets: Fluid chains and fishbones," *J. Fluid Mech.* **511**, 285 (2004).
- K. Ramamurthi, K. Nandakumar, and R. K. Patnaik, "Characteristics of sprays formed by impingement of a pair of liquid jets," *J. Propul. Power* **20**, 76 (2004).
- R. Li and N. Ashgriz, "Characteristics of liquid sheets formed by two impinging jets," *Phys. Fluids* **18**, 087104 (2006).
- H. M. Ryan, W. E. Anderson, S. Pal, and R. J. Santoro, "Atomization characteristics of impinging liquid jets," *J. Propul. Power* **11**, 135 (1995).
- S. Jung, S. D. Hoath, G. D. Martin, and I. M. Hutchings, "Atomization patterns produced by the oblique collision of two Newtonian liquid jets," *Phys. Fluids* **22**, 042101 (2010).
- M. R. O. Panão and J. M. D. Delgado, "Effect of pre-impingement length and misalignment in the hydrodynamics of multijet impingement atomization," *Phys. Fluids* **25**, 012105 (2013).
- B. Subedi, M. Son, S. P. Jang, and J. Koo, "Reliability study on skewness of doublet impinging injectors," *J. Mech. Sci. Technol.* **31**, 2295 (2017).
- N. D. Dombrowski and P. C. Hooper, "A study of the sprays formed by impinging jets in laminar and turbulent flow," *J. Fluid Mech.* **18**, 392 (1964).
- N. Yasuda, K. Yamamura, and Y. H. Mori, "Impingement of liquid jets at atmospheric and elevated pressures: An observational study using paired water jets or water and methylcyclohexane jets," *Proc. R. Soc. A* **466**, 3501 (2010).
- P. Zhang and B. Wang, "Effects of elevated ambient pressure on the disintegration of impinging sheets," *Phys. Fluids* **29**, 042102 (2017).
- L. Yang, Q. Fu, Y. Qu, B. Gu, and M. Zhang, "Breakup of a power-law liquid sheet formed by an impinging jet injector," *Int. J. Multiphase Flow* **39**, 37 (2012).
- S. Y. Jejurkar, G. Yadav, and D. P. Mishra, "Visualizations of sheet breakup of non-Newtonian gels loaded with nanoparticles," *Int. J. Multiphase Flow* **100**, 57 (2018).

- ²²X. Chen and V. Yang, "Recent advances in physical understanding and quantitative prediction of impinging-jet dynamics and atomization," *Chin. J. Aeronaut.* **32**, 45 (2019).
- ²³Y. Shen and D. Poulidakos, "Thickness variation of a liquid sheet formed by two impinging jets using holographic interferometry," *J. Fluids Eng.* **120**, 482 (1998).
- ²⁴D. Hasson and R. E. Peck, "Thickness distribution in a sheet formed by impinging jets," *AIChE J.* **10**, 752 (1964).
- ²⁵Y. J. Choo and B. S. Kang, "The velocity distribution of the liquid sheet formed by two low-speed impinging jets," *Phys. Fluids* **14**, 622 (2002).
- ²⁶C. S. Vegad, A. Kumar, and S. R. Chakravarthy, "Dynamics of free-surface mutually perpendicular twin liquid sheets and their atomization characteristics," *Phys. Fluids* **31**, 082103 (2019).
- ²⁷J. C. P. Huang, "The break-up of axisymmetric liquid sheets," *J. Fluid Mech.* **43**, 305 (1970).
- ²⁸W. E. Anderson, H. M. Ryan, and R. J. Santoro, "Impact wave-based model of impinging jet atomization," *Atom. Sprays* **16**, 791 (2006).
- ²⁹C. Inoue, T. Watanabe, and T. Himeno, "Study on atomization process of liquid sheet formed by impinging jets," AIAA Paper 2008-4847, 2008.
- ³⁰M. Arienti, X. Li, M. C. Soteriou, C. A. Eckett, M. Sussman, and R. J. Jensen, "Coupled level-set/volume-of-fluid method for simulation of injector atomization," *J. Propul. Power* **29**, 147 (2013).
- ³¹X. Chen, V. Yang, and S. Popinet, "High-fidelity simulations of impinging jet atomization," *Atom. Sprays* **23**, 1079 (2013).
- ³²X. Chen and V. Yang, "Direct numerical simulation of multiscale flow physics of binary droplet collision," *Phys. Fluids* **32**, 062103 (2020).
- ³³J. W. Bennowitz and R. A. Frederick, "Overview of combustion instabilities in liquid rocket engines - coupling mechanisms & control techniques," in *49th AIAA Joint Propulsion Conference* (AIAA, 2013).
- ³⁴H. P. Gadgil and B. N. Raghunandan, "Effect of skewness on the characteristics of impinging jet," *Atom. Sprays* **19**(1), 1 (2009).
- ³⁵S. Popinet, "Gerris: A tree-based adaptive solver for the incompressible Euler equations in complex geometries," *J. Comput. Phys.* **190**, 572 (2003).
- ³⁶C. W. Hirt and B. D. Nichols, "Volume of fluid (VOF) method for the dynamics of free boundaries," *J. Comput. Phys.* **39**, 201 (1981).
- ³⁷S. Popinet, "An accurate adaptive solver for surface-tension-driven interfacial flows," *J. Comput. Phys.* **228**, 5838 (2009).
- ³⁸A. J. Chorin, "Numerical solutions of the Navier–Stokes equations," *Math. Comput.* **22**, 745 (1968).
- ³⁹J. B. Bell, P. Colella, and H. Glaz, "A second-order projection method for the incompressible Navier–Stokes equations," *J. Comput. Phys.* **85**, 257 (1989).
- ⁴⁰X. Chen, P. Khare, and V. Yang, "Atomization patterns and breakup characteristics of liquid sheets formed by two impinging jets," in *49th AIAA Aerospace Sciences Meeting* (AIAA, 2011).
- ⁴¹X. Chen and V. Yang, "Mechanism Study of Impact Wave in Impinging Jets Atomization," in *50th AIAA Aerospace Sciences Meeting* (AIAA, 2012).
- ⁴²W. E. Anderson, H. M. Ryan, S. Pal, and R. J. Santoro, "Fundamental studies of impinging liquid jets," in *30th AIAA Aerospace Sciences Meeting* (AIAA, 1992).
- ⁴³C. I. Pairetti, S. M. Damián, N. M. Nigro, S. Popinet, and S. Zaleski, "Mesh resolution effects on primary atomization simulations," *Atom. Sprays* **30**, 913 (2020).
- ⁴⁴Z. Xu, T. Wang, and Z. Che, "Droplet deformation and breakup in shear flow of air," *Phys. Fluids* **32**, 052109 (2020).
- ⁴⁵D. Ayyappan, A. Vaidyanathan, C. Muthukumar, and K. Nandakumar, "Transition of subcritical liquid jets in single and multicomponent systems," *Phys. Fluids* **30**, 104106 (2018).
- ⁴⁶N. Sharma, W. D. Bachalo, and A. K. Agarwal, "Spray droplet size distribution and droplet velocity measurements in a firing optical engine," *Phys. Fluids* **32**, 023304 (2020).
- ⁴⁷H. Cong, L. Qian, Y. Wang, and J. Lin, "Numerical simulation of the collision behaviors of binary unequal-sized droplets at high Weber number," *Phys. Fluids* **32**, 103307 (2020).
- ⁴⁸H. Wu, F. Zhang, and Z. Zhang, "Droplet breakup and coalescence of an internal-mixing twin-fluid spray," *Phys. Fluids* **33**, 013317 (2021).